Characteristics of airborne black carbon-containing particles during the 2021 summer COVID-19 lockdown in a typical Yangtze River Delta city, China

Yuan Dai[1,2,3], Junfeng Wang[1,2], Houjun Wang[3], Shijie Cui[1,2], Yunjiang Zhang[1,2],

Haiwei Li[1,2], Yun Wu[1,2], Ming Wang[1,2], Eleonora Aruffo[5], Xinlei Ge[1,2,4*]

[1]Jiangsu Key Laboratory of Atmospheric Environment Monitoring and Pollution Control, Collaborative Innovation Center of Atmospheric Environment and Equipment Technology, School of Environmental Science and Engineering, Nanjing University of Information Science and Technology, Nanjing 210044, China
[2]International Joint Laboratory on Climate and Environment Change (ILCEC), Nanjing University of Information Science and Technology, 210044 Nanjing, China
[3]Yangzhou Environmental Monitoring Center, Yangzhou 225009, China
[4]School of Environment and Energy Engineering, Anhui Jianzhu University, Hefei 230601, China
[5]Department of Advanced Technologies in Medicine & Dentistry, University "G. d'Annunzio" of Chieti-Pescara; Center for Advanced Studies and Technology-CAST, Chieti 66100, Italy

Correspondence: Xinlei Ge (caxinra@163.com)

Abstract

Black carbon-containing particles (BCc) are ubiquitous in ambient air, significantly contributing to particulate matter (PM) pollution. The unexpected outbreak of the COVID-19 pandemic in the summer of 2021 prompted a localized and prolonged lockdown in Yangzhou City, situated in the Yangtze River Delta, China. This lockdown led to significantly altering in local anthropogenic emissions, while neighboring cities continued regular operations, providing a unique opportunity for the investigation of BCc characteristics influenced by varying emission conditions. Single particle aerosol mass spectrometer (SPA-MS) analysis revealed a notable decrease in the proportion of freshly emitted BCc during the lockdown period (LD). However, we did observe a concurrent 7% increase in $PM_{2.5}$ concentration during LD, with a higher proportion of aged BCc compared to the period before the lockdown (BLD). Evidence shows that regional transportation plays a vital role in the enhancement of $PM_{2.5}$ during LD. Moreover, reactive trace gases (e.g., NO_x, SO_2, and VOCs) could form thick coatings on pre-existing particles likely via enhanced heterogeneous hydrolysis under high RH as well, resulting in significant BCc particle growth (~600 nm), as well as $PM_{2.5}$, during LD. Our study highlights that short-term, strict local emission controls may not effectively reduce PM pollution due to the complex production and transmission characteristics of BCc and the non-linear responses of $PM_{2.5}$ to its precursors. Achieving further effective $PM_{2.5}$ reduction mandates a focus on nuanced control of BCc and necessitates a comprehensive and extensive approach with a regionally coordinated and balanced control strategy through joint regulation.

1. Introduction

China has implemented long-term clean air measures to cut down anthropogenic emissions and improve air quality (Ge et al., 2020), resulting in a nationwide reduction of average fine particulate matter ($PM_{2.5}$, aerodynamic diameter ≤ 2.5 μm) level from 50 μg m^{-3} in 2015 to 30 μg m^{-3} in 2020 (Zhou et al., 2022). However, this $PM_{2.5}$ concentration remains significantly higher than the new World Health Organization (WHO) guideline value of 5 μg m^{-3} (*WHO Global Air Quality Guidelines*, 2021).

Black carbon (BC) is a ubiquitous component of aerosols, typically constituting a small proportion (5~10%) of $PM_{2.5}$ in the atmosphere (Chen et al., 2020). However, freshly emitted BC evolves into BC-containing particles (BCc) by undergoing atmospheric aging, contributing to a rise in the total mass of $PM_{2.5}$ through processes of coating or embedding by other materials (Bond and Bergstrom, 2006; Peng et al., 2016). The number and mass fraction of BCc can excess 60% and 50% of $PM_{2.5}$, respectively, emphasizing the significant role of BC in elevating the mass concentration of particulate matter (PM) (Sun et al., 2022; Xie et al., 2020; Chen et al., 2020).

The atmospheric aging of BCc involves intricate chemical and physical transformations that influence their mixing state, morphology, hygroscopicity, and optical properties, all of which have profound implications for climate and human health (Bond et al., 2013; Ramanathan et al., 2008). For example, freshly emitted BC particles are initially hydrophobic but possess a porous surface structure that facilitates the internal or external mixing with co-emitted primary organic/inorganic and secondary materials that are associated with BC (Cheng et al., 2012; Li et al., 2020). On the other hand, BCc undergoes continually aging processes, including the condensation of low-volatility vapors (Li et al., 2022), coagulation with preexisting aerosols (Kondo et al., 2011), and heterogeneous oxidation with gaseous pollutants (Zhang et al., 2024). This alteration may affect the coating thickness, morphology, size distribution, and hygroscopicity of BCc, thereby impacting their climate forcing as well as atmospheric lifetime (Luo et al., 2022; Taylor et al., 2014). High loading of atmospheric BCc could also depress the development of the planetary boundary layer and exacerbate PM pollution episodes (Huang et al., 2018). BCc characteristics are influenced by various combustion sources and emission conditions, including local industrial burning, vehicle exhausts, residential coal burning, and biomass burning (Li et al., 2020; Sedlacek et al., 2022; Zhang et al., 2018), as well as long-range transport from other regions (Adachi et al., 2014; Zhang et al., 2021). Those diverse conditions complicate the development of parameterizations of BCc properties, the insufficient understanding of complex emission sources, aging processes, and physical properties of BCc, hampering the effectiveness of air quality remediation (Cappa et al., 2019; Kahnert, 2010; Sun et al., 2021).

Studies on the effects of large-scale and short-term stringent emission control events on air quality in China have been widely deployed, e.g., the 2008 Beijing Olympic Games (Wang et al., 2010; Zhou et al., 2010), the 2015 Asia-Pacific Economic Cooperation (APEC) (Zhu et al., 2015), the 2014 Nanjing Youth Olympic Games (Wang et al., 2022) and the national COVID-19 lockdown in 2020 winter (Huang et al., 2021; Le et al., 2020; L. Li et al., 2020; Wang et al., 2020). Previous studies extensively investigated air pollutant variations during the COVID-19 lockdown in the winter of 2020 across different regions of the world. Stringent restrictions on industrial and vehicular activities have resulted in significant reductions in gaseous pollutants and particulate matter, not only in megacities (Chen et al., 2020; Jeong et al., 2022; Sun et al., 2020) but also in middle-sized cities (Clemente et al., 2022; Wang et al., 2021; Xu et al., 2020) and rural areas (Cui et al., 2021, 2020; Jain et al., 2021). Compared to the decreasing trends observed in most cities worldwide, the level of $PM_{2.5}$ in Shanghai (Chang et al., 2020), Hohhot (Zhou et al., 2022), and the Northeast of China Plain (Nie et al., 2021) increased unexpectedly. These observations reveal the complex aerosol chemistry of $PM_{2.5}$ comprising primary and secondary components. The reduction of primary pollutants during lockdown resulted in a shift towards a higher proportion of secondary aerosols, including inorganic and organic species, exhibiting a non-linear response to emission changes (Zhang et al., 2021). Furthermore, some studies suggested that the increase in secondary aerosols during lockdown is due to the enhanced atmospheric oxidative capacity resulting from the rise in ozone levels (Y. Wang et al., 2021), unfavorable meteorological conditions (Chien et al., 2022; Sulaymon et al., 2021a), changes of local and regional emission sources (Feng et al., 2022). However, most previous studies focused on lockdown events during the cold seasons, and studies on summer lockdown events in China were very limited.

Yangzhou is located in the central region of the Yangtze River Delta (YRD), at the junction of the Yangtze River and, the Beijing-Hangzhou Grand Canal, which serves as a prominent economic city, industrial-intensive area, and highly active inland shipping node in East China. Due to the complex emissions and feedback with the East Asian monsoons (Ding et al., 2019), this region is susceptible to anthropogenic aerosols, especially BCc originating from chemical, steelmaking, coal-fired, petrochemical enterprises, and transportation, etc. Extensive studies have investigated the responses of atmospheric pollutants to emission changes during the COVID-19 lockdown measures in the YRD (Chen et al., 2021; L. Li et al., 2020; Qin et al., 2021; K. Zhang et al., 2022). However, the key chemical and physical processes specifically responsible for the BCc in this region are still unclear. During the summer of 2021, Yangzhou experienced a resurgence of COVID-19 with over 500 confirmed cases. In response, stringent public health measures were imposed from July 28th to September 10th, including the closure of public transport, and suspension of non-essential industrial plants, restaurants, shopping malls, and entertainment clubs. People were also mandated to quarantine at home. Unlike the nationwide COVID-19 lockdown in China

127   during the cold season of 2020 (Le et al., 2020; Sulaymon et al., 2021b), the summer
128   lockdown in Yangzhou was more localized but protracted, significantly altering local
129   anthropogenic emissions while neighboring cities maintained regular operations, which
130   provides a unique opportunity to explore and compare the diverse mixing states and,
131   the aging process of BCc in different anthropogenic emission conditions in summer.
132
133   Here we report the chemical compositions and aging characteristics of airborne BCc in
134   YRD. Our investigation involved a combination of ground measurements, spaceborne
135   observations, and mass spectrometric analysis conducted during the COVID-19
136   lockdown in the summer of 2021 in Yangzhou. Additionally, we employed potential
137   source contribution function (PSCF) analysis to investigate the air pollution patterns in
138   the YRD.
139

2. Methods

140

2.1 Sampling site and instruments

141

142   The in-situ online measurements were conducted at a rooftop laboratory 20 m above
143   ground located in a national air quality monitoring station, Yangzhou Environmental
144   Monitoring Center (32.41ºN, 119.40ºE), Yangzhou, China (**Figure 1**). This sampling
145   site is a typical urban site surrounded by residential areas, arterial roads, parks,
146   restaurants, and shopping centers. In this study, the measurement period was divided
147   into three phases: the before-lockdown period (BLD: 30 June to 27 July 2021), the
148   lockdown period (LD: 28 July to 9 September 2021), and the after-lockdown period
149   (ALD: 10 September to 7 October 2021) (**Figure 2**).
150
151   A single-particle aerosol mass spectrometer (SPA-MS, Hexin Analytical Instrument Co.,
152   Ltd., China) was deployed during the field campaign to obtain the chemical
153   composition, size distribution, and mixing state of individual $PM_{2.5}$ particles. A cyclone
154   with a 2.5 μm cutpoint (Model URG-2000-30ED) and a Nafion dryer is equipped in
155   front of the sampling inlet. Individual particles are introduced into the SPA-MS through
156   a critical orifice at a flow rate of 3 L min^{-1}. The vacuum aerodynamic diameters (D_{va})
157   are determined using the velocities derived from two continuous laser beams (diode Nd:
158   YAG, 532 nm) spaced 6 cm apart. Subsequently, these particles are desorbed and
159   ionized by a downstream pulsed laser (266 nm), and ion fragments are generated and
160   measured by a Z-shaped bipolar time-of-flight mass spectrometer. A more detailed
161   description of SPA-MS can be found in previous studies (Li et al., 2011).
162
163   $PM_{2.5}$ mass concentration was measured by a particulate matter monitor (XHPM2000E,
164   Xianhe, China). Nitrogen oxides (NO_x = NO + NO_2), $SO_{2,}$ and ozone (O_3)
165   concentrations were detected with a set of Thermo Fisher Scientific instruments
166   (Models 42i, 43i, and 49i). The concentrations of 103 volatile organic compounds
167   (VOCs) in ambient air, comprising 57 ozone precursors (PAMS), 12 aldehydes and

168   ketones, and 34 toxic organics (TO15), were continuously monitored at hourly intervals
169   using an online device (TH-300B, Tianhong, China). Meteorological parameters,
170   including ambient temperature (T), relative humidity (RH), precipitation (PCP), wind
171   direction (WD), and wind speed (WS) were observed synchronously using an automatic
172   weather instrument (WXT530, Vaisala, Finland). All online data presented in this paper
173   were hourly averaged at local time (Beijing time, UTC+8).
174

175 2.2 Data analysis

176 2.2.1 Satellite Product

177   In this study, we utilized the Copernicus Atmosphere Monitoring Service (CAMS)
178   Global Near-Real-Time dataset (available at https://developers.google.com/earth-
179   engine/datasets/catalog/ECMWF_CAMS_NRT), acquired from the European Centre
180   for Medium-Range Weather Forecasts (ECMWF), to analyze the distribution of total
181   surface column concentrations of NO_2, SO_2 and surface $PM_{2.5}$ mass concentration.
182   CAMS offers the capacity to continuously monitor the composition of the Earth's
183   atmosphere at global and regional scales since 2016, with a spatial resolution of 44528
184   meters (Benedetti et al., 2009; Morcrette et al., 2009). The details of the bands of the
185   dataset used in this study are shown in Table S2. We calculated and plotted the averaged
186   2-dimensional data of ECMWF/CAMS/NRT NO_2, SO_2, and $PM_{2.5}$ during BLD and LD
187   over the region of interest (17.93~54.74 ºN, 71.21~142.23 ºE) using Google Earth
188   Engine (Gorelick et al., 2017). The integration of remote sensing measurements has
189   provided a more comprehensive understanding of the sources and distributions of
190   particle matter and gaseous pollutants facilitating the evaluation of the impact of human
191   activities on air quality.

192 2.2.2 Geographic Source Analysis

193   The potential source contribution function (PSCF) analysis, based on the Hybrid
194   Single-Particle Lagrangian Integrated Trajectory (HYSPLIT) model, can be employed
195   to identify regional sources of air pollutants. Before conducting the PSCF analysis, 36
196   hours of air mass backward trajectories with one-hour resolution at 500 m above ground
197   level were calculated using the wind data from the Global Data Assimilation System
198   (GDAS) provided by the National Oceanic and Atmospheric Administration (NOAA)
199   (Wang et al., 2009). An open-source software MeteoInfo (Wang, 2014) was utilized for
200   the PSCF analysis. The whole study area (110.1~133.4 ºE and 21.3~39.9 ºN) covered
201   by the trajectories was divided into thousands of cells with a spatial resolution of 0.1°
202   × 0.1°. The PSCF was simulated according to the following equation:

$$203 \qquad PSCF_{ij} = \frac{m_{ij}}{n_{ij}} \qquad\qquad (1)$$

204   where $PSCF_{ij}$ is the conditional probability that the grid cell (i, j) was a source of the
205   species found in high concentration (Hopke et al., 1993); n_{ij} is the number of all
206   trajectories passing through this grid cell, and m_{ij} is the number of trajectories. In this
207   study, the pollution criterion values for different BCc particle types were set as the 75th

208 percentile of hourly average number fractions, respectively. To further improve the
209 accuracy of the PSCF analysis and minimize analytical uncertainties, the Weighted
210 PSCF (WPSCF) functions as shown in Equation (2~3) were applied (Polissar et al.,
211 1999). The weight (W_{ij}) for each grid cell was determined based on the number of
212 trajectory endpoints (n_{ij}) as follows:

213
$$WPSCF_{ij} = W_{ij} \times PSCF_{ij} \tag{2}$$

214
$$W_{ij} = \begin{cases} 1.00 & n_{ij} > 3n_{ave} \\ 0.70 & 1.5n_{ave} < n_{ij} \leq 3n_{ave} \\ 0.40 & n_{ave} < n_{ij} \leq 1.5n_{ave} \\ 0.17 & n_{ij} \leq n_{ave} \end{cases} \tag{3}$$

215 Here, n_{ave} is the average number of trajectory endpoints of each grid.

216 **2.2.3 SPA-MS Data Analysis**

217 In total, 1649574 particles were analyzed during the entire observation period. The size
218 and chemical composition of single particles were analyzed using the Computational
219 Continuation Core (COCO V1.4) toolkit in MATLAB 2022 (The MathWorks, Inc.).
220 Our focus was on BCc, which was identified based on the relative peak area (RPA) of
221 carbon ion clusters ($C_n^{\pm}$, n = 1, 2, 3, …), with a threshold of 0.05 (Zhang et al., 2021).
222 An adaptive resonance theory-based neural network algorithm (ART-2a) was applied
223 to classify the measured individual particles based on the presence and intensity of ion
224 peaks, with a vigilance factor of 0.75, a learning rate of 0.05, and 20 iterations (Song et
225 al., 1999).
226

3. Results and discussion

3.1 Field observations

229 **Figure 2** presents the temporal variations of meteorological parameters, $PM_{2.5}$, NO_x,
230 and SO_2 concentrations. Notably, $PM_{2.5}$, NO_x, and SO_2 were significantly reduced at
231 the end of BLD due to a high precipitation event, and the data collected during the
232 precipitation were excluded from the data analysis. During BLD, the mean temperature
233 (*T*) was 28±3 ℃, with an average relative humidity (RH) of 81±11%. The prevailing
234 winds originated from the south and southeast, with a mean wind speed (WS) of 3.4±
235 0.9 m s^{-1}. In comparison, LD shows a decline in temperature to 26±2 ℃ and WS to 2.3
236 ±0.8 m s^{-1}, but an increase in RH to 87±10%. **Figure S2b and c** present uniform
237 distributions of RH and boundary-layer height (BLH) across the YRD during LD. The
238 implication is that the resemblance of regional meteorological conditions in YRD and,
239 the effective removal of the pollutants accumulated at the end of BLD, provides a
240 favorable condition for investigating the regional transport of BCc during LD in
241 Yangzhou. During ALD, the temperature declined to 25±3 ℃, the WS increased to 3.2
242 ±1.4 m s^{-1}, and RH decreased to a lower level of 75±15%.
243

244   Surface concentrations of NO_x (19 µg m^{-3}) and TVOC (56 µg m^{-3}) were the lowest
245   during LD compared to those of BLD and ALD, whereas the surface O_3 concentration
246   showed an increase of 13 µg m^{-3} (19%) during LD compared to BLD. The reduction of
247   fresh NO emission alleviates O_3 titration (Steinfeld, 1998) could be an explanation.
248   Furthermore, analysis from **Figure S3** indicates that the O_3 level is higher than those
249   of neighboring cities in the YRD, suggesting higher atmospheric oxidation capacity
250   during LD. However, the average concentrations of $PM_{2.5}$ (19.9 vs. 21.2 µg m^{-3}), SO_2
251   (9.4 vs. 9.5 µg m^{-3}), CO (0.61 vs. 0.64 mg m^{-3}), and TVOC (58 vs. 56 µg m^{-3}) were
252   comparable during both BLD and LD (**Figure 3**).
253
254   After LD, social activities gradually resumed in Yangzhou City, leading to an apparent
255   increase in all observed pollutants during the ALD period. For instance, there were
256   relative increases of 71% for NO_x, 22% for SO_2, 55% for TVOC, 30% for O_3, 29% for
257   $PM_{2.5,}$ and 17% for CO from LD to ALD, respectively(**Figure 3**). Given that both BC
258   and CO are byproducts of incomplete combustion of carbon-containing fuels (Wang et
259   al., 2015), and the high correlation between BC and CO (Zhou et al., 2009), it is
260   plausible to infer that the primary emission source of BC during LD was different with
261   that during ALD.
262
263   Satellite-retrieved $PM_{2.5}$, NO_2, and SO_2 data over the entire region of eastern China
264   were also investigated, and results show that these pollutants were predominantly
265   concentrated in Shanghai and its neighboring cities, including Yangzhou, during both
266   BLD and LD (**Figure S4**). **Figure 4** presents regional fractional changes, including
267   Yangzhou, of mean $PM_{2.5}$, NO_2, and SO_2 concentrations from the BLD to LD periods
268   in YRD, all showing an increase of 29%, 6%, and 14%, respectively. In comparison,
269   Yangzhou city experienced lower increases in these air pollutants, with slight changes
270   of 6.0%, -18.0%, and -4.3% for $PM_{2.5}$, NO_2, and SO_2, respectively. The implication is
271   that, even though local primary emissions, such as NO_2, and SO_2, were reduced
272   substantially during LD, they still could be affected by regional transport. Furthermore,
273   as depicted in **Figure S3**, the concentrations of NO_2 in major cities of the YRD were
274   more than twice higher than in Yangzhou during LD, confirming a relatively lower local
275   primary emissions due to the stringent lockdown. However, the higher level of SO_2 in
276   Yangzhou during LD may be attributed to the nearby power stations along the Yangtze
277   River, which were not impacted by the lockdown measures.
278

279   ## 3.2 Chemical composition and size distribution of individual
280   ## BCc

281   Based on the SPA-MS analysis, a total of 1068362 BCc was collected during the whole
282   study period. The BCc accounted for 59%, 69%, and 57% of the total number of
283   measured particles in the BLD, LD, and ALD periods, respectively. **Figure 5** shows the
284   normalized average mass spectra of BCc during three periods. Ion height in each

285 spectrum reflects the number fraction of the detected BCc with the corresponding ion
286 to the total BCc, while colors represent peak area ranges of detected ions. BCc in BLD,
287 LD, and ALD shown similar mass spectra at $m/z < 100$, with common peaks including
288 carbon ion clusters ($C_n^\pm$, n = 1~7), m/z 27$[C_2H_3]^+$, 37$[C_3H]^+$, 43$[C_2H_3O]^+$, 51$[C_4H_3]^+$,
289 63$[C_5H_3]^+$, 46$[NO_2]^-$, 62$[NO_3]^-$, and 97$[HSO_4]^-$. However, the abundance of large m/z
290 carbon ions ($C_n^\pm$, n > 7) in both BLD and ALD periods was 1.5 times higher than that in
291 the LD. Previous studies have indicated that high-mass carbon ions may be linked to
292 traffic emissions, particularly those from diesel trucks(Xie et al., 2020; Liu et al., 2019),
293 and the observed reduction in such ions during LD suggests a decrease in local vehicle
294 emissions. This trend is also consistent with the changes observed in aromatic
295 compounds, e.g. m/z 119$[C_9H_{11}]^+$.

296

297 Further, BCc was classified into 12 types based on the differences in chemical features
298 and temporal variations, as shown in **Table S1**. Fresh BC particles (BC-fresh) are those
299 freshly emitted without undergoing significant atmospheric processing (Ding et al.,
300 2021). Five types of BC-fresh particles were identified according to their ion markers:
301 (i) BC-pure is dominated by carbon clusters ($C_n^\pm$) with minor ion signals of inorganic
302 species, such as m/z 46$[NO_2]^-$ and m/z 97$[HSO_4]^-$ from nitrate and sulfate, respectively
303 (Xie et al., 2020); (ii) BCc from biomass burning (BB) are characterized by ion signals
304 at m/z 39$[K]^+$, 45$[CHO_2]^-$, 59$[C_2H_3O_2]^-$, and 73$[C_3H_5O_2]^-$, with a relative peak area
305 (RPA) more than 0.5 (Silva et al., 1999); (iii) coal combustion BCc (CC) typically
306 include small carbon clusters ($C_n^\pm$, n = 1~4), metal elements (e.g., m/z 7$[Li]^+$, 23$[Na]^+$,
307 27$[Al]^+$, 56$[Fe]^+$, 63$[Cu]^+$ and 206/207/208$[Pb]^+$), and organic carbon (38$[C_3H_2]^+$,
308 43$[C_2H_3O]^+$) peaks in the positive mass spectrum, while the strong signals of secondary
309 inorganic species (46$[NO_2]^-$, 43$[AlO]^-$, 62$[NO_3]^-$, 80$[SO_3]^-$, 97$[HSO_4]^-$) in the
310 negative ion mode suggest that CC particles were long-distance transported or more
311 processed (Zhang et al., 2022; Zhang et al., 2009); (iv) particles from vehicle emission
312 (VE) are characterized by the presence of ion signals at m/z 40$[Ca]^+$, 51$[V]^+$, 55$[Mn]^+$,
313 67$[VO]^+$, 46$[NO_2]^-$, 62$[NO_3]^-$, and 79$[PO_3]^-$, as well as high loadings of organic
314 carbon (41$[C_3H_5]^+$, 43$[C_2H_3O]^+$) and carbon clusters ($C_n^\pm$, n = 1~4) ion peaks (Yang et
315 al., 2017); (v) BCc that are internally mixed with more than one type (BB, CC, and VE)
316 are categorized as Mix type (Sun et al., 2022).

317

318 Aged BC particles, denote as BC-aged, undergo a series of chemical reactions and
319 physical transformations. These processes typically lead to changes in their morphology,
320 hygroscopicity, and optical properties as they are coated with other materials (He et al.,
321 2015). Six types of BCc are classified as BC-aged and are further grouped into BCOC
322 and BC-SNA, depending on whether they contain mainly organic carbon (OC) or
323 sulfate/nitrate/ammonium (SNA). First, BCOC types indicate BC-aged particles that
324 are internally mixed with OC. These particles are characterized by the presence of
325 carbon clusters ($C_n^\pm$) and $C_nH_m^+$ ions (n = 1~6, m = 1~3) in positive mass spectra (Xie
326 et al., 2020). On the other hand, BC-aged particles that do not mix with OC are named

BC-SNA indicating the mix with secondary inorganic species. Additionally, BCOC particles with negative mass spectra dominated by nitrate ions ($46[NO_2]^-$ and $62[NO_3]^-$) or sulfate ions ($97[HSO_4]^-$) are referred to as BCOC-N or BCOC-S, respectively; otherwise, BCOC particles showing similar peak areas of nitrate and sulfate are named BCOC-SN. The BC-SNA particles are further categorized as BC-N, BC-S, and BC-SN based on similar principles. Note the remaining particles that cannot be classified into either BC-fresh or BC-aged ones are denoted as BC-other. More details of BCc particle types are shown in **Table S1** and **Figure S1** in the Supplement.

During BLD, the average number fraction of BC-fresh particles was 36% with sizes mainly concentrated at 500 nm, similar to the mode size of BC-aged particles was 520 nm (**Figure 6**). The predominant BCc types during BLD were BCOC-S and BC-S (24% and 12% by number), likely because sulfate was removed less efficiently than organic matter (OM) and NO_3 by heavy precipitation, especially during the warm seasons (Isokääntä et al., 2022). As shown in **Figures 6c and d**, the peak size of BC-SNA was larger than that of BCOC in all periods, indicating that organics coated BCc generally had a relatively thin coating compared to those coated by secondary inorganic species, which is consistent with previous studies (Sun et al., 2016; Wang et al., 2019).

During the transition of BLD to LD, heavy precipitation occurred from the evening to July 27th and early morning of July 28th (the eve of lockdown), resulting in the removal of a majority of the pollutants ($PM_{2.5}$: 4 μg m^{-3}, O_3: 35 μg m^{-3}, NO_x: 8 μg m^{-3}). After that, strict lockdown were carried on and the primary emissions were abruptly cut down. As a result, the number fraction of BC-fresh particles significantly decreased from 37% to 28% and that of VE-type particles dropped from 12% to 3% (by number). Expectedly, with the decrease in NO_x, an obvious enhancement of O_3 was observed during LD (**Figure 3**). According to previous studies (Huang et al., 2021; Laughner et al., 2021), large reduction of NO_x may promote the formation of O_3 under a VOC-limited regime and enhance the oxidation capacity of the local atmosphere, which may promote the number fraction of BC-aged particles increased from 64% in the BLD to 72% in LD (**Figure 7a**), indicating the lockdown could accelerate aging of BCc through complicated chemical reactions and/or physical coagulation. Additionally, the most abundant type of BCc changed from BCOC-S (24% by number) in the BLD to BC-N (25%) in the LD (**Figure 7a**), suggesting different BCc formation pathways. Despite the abrupt reductions of NO_x due to the city lockdown, it should be aware that the $PM_{2.5}$ concentration slightly increased during LD, highlighting the non-linear relationship between primary emissions and $PM_{2.5}$ levels.

During ALD ($PM_{2.5}$: 26 μg m^{-3}, NO_x: 28 μg m^{-3}, TVOC: 76 μg m^{-3}), the number fraction of BC-fresh particles rose from 28% (LD) to 31% (ALD), while the fraction of VE particles also increased from 3% (LD) to 12% (ALD) (**Figure 7a**). Notably, the size distributions of BC-fresh and BC-aged particles presented relatively small peaks at 690

369 nm and 820 nm during ALD, in addition to the prominent peaks at 490 nm and 500 nm,
370 which were different from those in the BLD and LD periods. These small peaks were
371 relatively close to the dominant sizes of BC-fresh and BC-aged particles during LD
372 (**Figure 6**). This result suggests that a substantial number of BCc with small sizes
373 (around 500 nm) after the lockdown was lifted in Yangzhou, owing to the sudden
374 enhancement of primary emissions; on the other hand, particles with large diameters
375 (>690 nm) may have formed due to the participation of more trace reactive gases (e.g.,
376 NO_x, SO_2, and VOCs) in continuous aging reactions, resulting in thicker coatings on
377 the surface of pre-existing particles and therefore a more clear separation of two-mode
378 sizes during the ALD period than during the other two periods. This hypothesis was
379 also supported by the increased number fraction of BCOC-SN during the ALD period
380 (Figure 7a). Similar findings have been reported in the North China Plain (NCP) and
381 the YRD during cold seasons, where thicker coatings on secondary aerosols were also
382 observed under lower RH (<70%) (Zhang et al., 2021). This might be due to that
383 particles with more organics and nitrate can result in earlier deliquescence and provide
384 aqueous surfaces that facilitate the heterogeneous formation of secondary species under
385 relatively low RH (Zhang et al., 2021). Among the three periods, the difference between
386 the mode sizes of BC-aged and BC-fresh particles was the smallest (10 nm) during the
387 ALD period (Figure 6a and b). This size reduction can be attributed to the increased
388 BCOC and hydrophobic primary particles after lockdown (Figure 7). Because the
389 internally mixed BCOC and hydrophobic primary particles may constrain further
390 growth of secondary BC-SNA particles (Liu et al., 2016; Zhang et al., 2018), thereby
391 leading to smaller-sized BC-aged particles. Moreover, the differences in BCc mode
392 sizes between ALD and BLD periods also reveal an interesting fact that the lockdown
393 effect may not only affect air quality during lockdown but also can influence the air
394 quality even after lockdown, as the resumed emissions after lockdown may be subjected
395 to different chemistry from that before lockdown.
396
397 Throughout the entire observation, the changes in the number fraction of BC-SNA
398 exhibited consistency with the variations in RH (**Figure 7b**), indicating that BC tends
399 to mix with ammonium sulfate and ammonium nitrate under high RH conditions.
400 Meanwhile, the number fraction of BCOC shows similar patterns as TVOC, suggesting
401 that high TVOC levels may facilitate the coating of organics on BC cores under low
402 RH condition. **Figure 8** displays the number fraction of BCc species as a function of
403 $PM_{2.5}$. Overall, as $PM_{2.5}$ levels increased, the number fraction of BC-aged particles also
404 increased, while the proportion of BC-fresh particles decreased during BLD and LD,
405 indicating a clear transition from BC-fresh particles to more aged ones, in line with the
406 average size distribution during ALD has a small peak at 900 nm. Specifically, the
407 increase in $PM_{2.5}$ was driven by BCOC-S during BLD (**Figure 8a**), whereas BC-N
408 played a vital role in the $PM_{2.5}$ increase during LD (**Figure 8b**). Interestingly, the
409 concentration of NO_x, the primary precursor of BC-N, decreased by 31% and 41%
410 during LD compared to BLD and ALD, respectively (**Figure 3**), indicating a strong

411 non-linear response of nitrate in BCc to NO_x, likely due to much faster conversion of
412 NO_x to nitrate upon enhanced atmospheric oxidation capacity; additionally, the high
413 proportion of BC-N during LD might be attributed to regional transport, similar to that
414 in Shanghai during 2020 winter lockdown (Chang et al., 2020).
415

3.3 Chemical aging of BCc

417 As shown in **Figure 5**, in the average positive mass spectra of total BCc, the peak areas
418 of C_n^+, OM, and metals contributed to more than 95% of the total, while nitrate and
419 sulfate peak areas accounted for more than 90% of the negative mass spectral signal.
420 To better elucidate the aging processes of BCc during different lockdown periods, we
421 summed the carbon clusters $C_n^\pm$ (n = 1~5, accounting for more than 99% of C_n) peak
422 areas to represent BC, and the total peak area of sulfate, nitrate, and ammonium (SNA)
423 to represent the second inorganic components coated on BC. Additionally, we defined
424 the sum of positive peak areas, excluding C_n^+ and metals, as OC to represent the OM
425 coated on BC. These peak areas encompassed almost all the coating materials, except
426 for metals, of BCc. The changes in the mixing state and morphology of BCc can provide
427 insights into their aging characteristics, as reported previously (Kandler et al., 2018;
428 Moffet et al., 2013). In this study, we use OC/C_n and SNA/C_n ratios to describe different
429 types of chemical components coated on BC-fresh, and we use the ratio of the mode
430 size of BC-aged (D_{aged}) to that of contemporaneous BC-fresh (D_{fresh}) to represent the
431 aging degree of BCc.
432

433 **Figure 9** illustrates the diurnal variations of the OC/C_n and SNA/C_n ratios along with
434 the size distribution of BCc during different periods. We observed that both OC/C_n and
435 SNA/C_n increased during nighttime and decreased during daytime. These variations
436 showed the prominent enhancements of nocturnal OM and SNA, which could be
437 attributed to the accelerated gas-to-particle partitioning and nocturnal secondary
438 formation of organic/inorganic components under high relative humidity (RH > 85%)
439 and relatively stagnant air mass (WS < 3 m s^{-1}) (**Figure S5**). It is worth noting that from
440 BLD to LD and ALD, the intensity of diurnal variations of OC/C_n and SNA/C_n
441 increased obviously. This discrepancy can be attributed to several reasons. (i) During
442 BLD, the frequent precipitations effectively scavenged the particles (Isokääntä et al.,
443 2022); (ii) In contrast, stronger solar radiation and higher O_3 concentration during LD
444 promoted photochemical formations of OC and SNA; (iii) After lockdown, more
445 precursors due to increased local emissions may lead to more production of secondary
446 components than that during BLD as explained earlier. These results indicate that the
447 aging process and mixing state of BCc depend strongly on meteorological conditions
448 as well as emission sources in urban cities.
449

450 As shown in **Figure 9**, BCc with ~400 nm D_{va} exhibited significant diurnal fluctuations
451 in the OC/C_n and SNA/C_n ratios, during LD. There is a noticeable increase in the
452 proportion of BC-SNA particles during nighttime when RH is relatively high. These

observations suggest that nighttime heterogeneous hydrolysis may be considered a key mechanism responsible for the formation of BCOC and BC-SNA particles. According to Jacobson (2002), coagulation can be significant between particles with sizes <100nm and >1μm but insignificant for particles of >300nm, when the total particle number concentration is higher than 10^4 cm^{-3}. During LD, the OC/C_n and SNA/C_n ratios of BCc with ~400 nm D_{va} exhibited pronounced diurnal variations (**Figure 9**) and the number fraction of BC-SNA increased obviously. Despite the difference between D_{va} and physical diameter, such results imply that chemical reactions should be considered as the major pathway for BCOC and BC-SNA particles of ~400 nm D_{va}, while the large-sized BC-aged particles (>1 μm) may be partially from physical coagulation. Additionally, the larger mode peak (600 nm, D_{va}) and higher D_{aged}/D_{fresh} ratios (1.11) were observed compared to those of BLD (510 nm, 1.03) and ALD (500 nm, 1.02) (**Figure 6**). Since RH was significantly higher during LD (average RH of 87%) than BLD (average RH of 81%) and ALD period (average RH of 75%), this result again supports that aqueous or heterogeneous reactions might play a more important role to facilitate the chemical conversion of trace reactive gases (e.g., SO_2, NO_x, and VOCs) and then formed a thicker coating on the surfaces of BC cores, leading to evident growth in the size of BCc. This aqueous or heterogeneous process during LD likely converted partially coated particles to fully thickly coated BCc as well.

3.4 Source apportionment of BCc during lockdown

In addition to local emissions, regional transport plays a significant role in influencing pollutant levels. The emergent lockdown in Yangzhou led to strict limitation on local emissions, while surrounding cities were still running as usual. This is supported by **Figure S6**, which illustrates the PM$_{2.5}$ concentrations in Yangzhou and the other five surrounding YRD cities (e.g., Nanjing, Zhenjiang, Changzhou, Taizhou, and Chuzhou) during the campaign. High correlations between PM$_{2.5}$ concentrations in Yangzhou and the other five cities were observed across all different periods (**Figure S6**). These findings underscore the importance of the regional transport in PM$_{2.5}$ pollution during the campaign, providing an unique opportunity to investigate the transmission and source characteristics of BCc in YRD during summer. Herein, PSCF analysis was applied to qualitatively simulate the source probability distributions of the specific BCc particle types (BC-fresh, BC-aged, BCOC, and BC-SNA) during LD.

As shown in **Figure 10**, the hotspots of potential sources for the four particle types exhibited strong agreements with each other and primarily concentrated in the southeast of Yangzhou, especially along the coast of the Yangtze River, with the WPSCF greater than 0.6. These hotspot areas also encompassed chemical enterprises, power plants, petrochemical industrial parks, and the Yangtze River in the YRD. This evidence suggests that the region of southeast Yangzhou and lower reaches of the Yangtze River are major source areas for the regionally transported BCc in Yangzhou during lockdown. Additionally, Luo et al. (2023) reported that regional transport of pollutants can occur

near the surface from upwind areas when the wind speed (WS) exceeds 2 m s^{-1}. **Figure S5b** shows that the mean daytime WS was 3 m s^{-1}, indicating that both BC-fresh and BC-aged particles, along with trace gases (e.g., SO_2, NO_x, and VOCs), originating from the hotspot areas, could be transported effectively to Yangzhou. Additionally, the average size of BCc remained around 600 nm at daytime (**Figure S5c**), suggesting that BCc could undergo continual aging reactions under relatively lower RH, but produce relatively thinly coated BCc with smaller sizes than those at nighttime (average size of 650 nm). The mean nocturnal WS decreased to 2 m s^{-1}, indicating that the regional atmosphere becomes stagnant (**Figures S5a, b**). As mentioned earlier and underscored here again, this stagnant and humid atmospheric condition may promote aqueous or heterogeneous reactions, likely further leading to the production of more thickly coated BCc than daytime ones.

4. Conclusions and implications

During the summer of 2021, the COVID-19 lockdown imposed in Yangzhou resulted in a significant decrease in anthropogenic emissions from traffic and manufacturing sectors. To examine the effects of this lockdown, we utilized spaceborne observations, ground-based measurements, and particularly SPA-MS analysis to explore the variations, aging characteristics, and sources of BCc in the YRD. We showed that the strict emission controls effectively reduced local gaseous pollutants. However, the decline in NO_x (-30%) and TVOC (-5%) levels might on the other hand result in increased O_3 (+19%), leading to a rise in BC-aged particles and a slight elevation in $PM_{2.5}$ levels during the lockdown. Our results revealed a strong non-linear response of $PM_{2.5}$ and O_3 to the gaseous precursors.

The SPA-MS analysis results further demonstrate significant enhancement of OM and SNA coating species on BC-fresh particles, owing to gas-to-particle partitioning and nocturnal multiphase chemistry. Consequently, we observed a higher fraction of BC-aged particles (73%) during the lockdown due to enhanced oxidizing capacity and high relative humidity (RH > 85%). The BC-fresh particles tended to mix with SNA under high RH conditions, while high TVOC levels were accompanied by BCOC formation. However, BCOC particles generally exhibited smaller sizes compared to BC-SNA particles. Moreover, we propose that aqueous or heterogeneous reactions might be important to generate BCOC and BC-SNA particles, especially ones with 400 nm D_{va}, while coagulation might play a more prominent role in larger BC-aged particles. The aging process during LD promoted the conversion of partly coated particles to totally coated ones, with larger diameters (600 nm) and thicker coatings.

It should be noted that the observed average $PM_{2.5}$ concentration during the lockdown in Yangzhou was 21 μg m^{-3}, which still significantly exceeds the WHO's air quality guideline of 5 μg m^{-3}. Our research underscores the crucial role of BCc, which

536 constitutes a significant portion of $PM_{2.5}$, in particulate matter pollution. These particles
537 originate from diverse combustion sources and their behavior is intricately influenced
538 by complex chemistry, regional transport, and meteorological factors. Mere reductions
539 in local primary emissions from traffic and manufacturing sectors exhibit limited
540 efficacy in air quality improvement. Therefore, effective air quality remediation
541 strategies necessitate nuanced control of BCc alongside broader emission reduction
542 efforts. We suggest a more comprehensive regulation of precursor gases from multiple
543 sectors, a wide-ranging joint regulation approach as well as proper consideration of the
544 chemistry, to develop an effective strategy for air quality improvement.

References

Adachi, K., Zaizen, Y., Kajino, M., Igarashi, Y., 2014. Mixing state of regionally transported soot particles and the coating effect on their size and shape at a mountain site in Japan. Journal of Geophysical Research: Atmospheres 119, 5386–5396. https://doi.org/10.1002/2013JD020880

Benedetti, A., Morcrette, J.-J., Boucher, O., Dethof, A., Engelen, R.J., Fisher, M., Flentje, H., Huneeus, N., Jones, L., Kaiser, J.W., Kinne, S., Mangold, A., Razinger, M., Simmons, A.J., Suttie, M., 2009. Aerosol analysis and forecast in the European Centre for Medium-Range Weather Forecasts Integrated Forecast System: 2. Data assimilation. Journal of Geophysical Research: Atmospheres 114. https://doi.org/10.1029/2008JD011115

Bond, T.C., Bergstrom, R.W., 2006. Light Absorption by Carbonaceous Particles: An Investigative Review. Aerosol Science and Technology 40, 27–67. https://doi.org/10.1080/02786820500421521

Bond, T.C., Doherty, S., Fahey, D.W., Forster, P., Berntsen, T., DeAngelo, B., Flanner, M., Ghan, S., Kärcher, B., Koch, D., Kinne, S., Kondo, Y., Quinn, P.K., Sarofim, M., Schultz, M., Michael, S., Venkataraman, C., Zhang, H., Zhang, S., Zender, C.S., 2013. Bounding the role of black carbon in the climate system: A Scientific assessment. Journal of Geophysical Research: Atmospheres 118, 5380–5552. https://doi.org/10.1002/jgrd.50171

Cappa, C.D., Zhang, X., Russell, L.M., Collier, S., Lee, A.K.Y., Chen, C.-L., Betha, R., Chen, S., Liu, J., Price, D.J., Sanchez, K.J., McMeeking, G.R., Williams, L.R., Onasch, T.B., Worsnop, D.R., Abbatt, J., Zhang, Q., 2019. Light Absorption by Ambient Black and Brown Carbon and its Dependence on Black Carbon Coating State for Two California, USA, Cities in Winter and Summer. Journal of Geophysical Research: Atmospheres 124, 1550–1577. https://doi.org/10.1029/2018JD029501

Chang, Y., Huang, R., Ge, X., Huang, X., Hu, J., Duan, Y., Zou, Z., Liu, X., Lehmann, M.F., 2020. Puzzling Haze Events in China During the Coronavirus (COVID-19) Shutdown. Geophys. Res. Lett. 47. https://doi.org/10.1029/2020GL088533

Chen, H., Huo, J., Fu, Q., Duan, Y., Xiao, H., Chen, J., 2020. Impact of quarantine measures on chemical compositions of PM2.5 during the COVID-19 epidemic in Shanghai, China. Science of The Total Environment 743, 140758. https://doi.org/10.1016/j.scitotenv.2020.140758

Chen, L., Qi, X., Nie, W., Wang, J., Xu, Zheng, Wang, T., Liu, Y., Shen, Y., Xu, Zhengning, Kokkonen, T., Chi, X., Aalto, P., Paasonen, P., Kerminen, V.-M., Petäjä, T., Kulmala, M., Ding, A., 2021. Cluster Analysis of Submicron Particle Number Size Distributions at the SORPES Station in the Yangtze River Delta of East China. Journal of Geophysical Research: Atmospheres 126. https://doi.org/10.1029/2020JD034004

Chen, L., Zhang, F., Yan, P., Wang, X., Sun, L., Li, Y., Zhang, X., Sun, Y., Li, Z., 2020. The large proportion of black carbon (BC)-containing aerosols in the urban

atmosphere. Environmental Pollution 263, 114507. https://doi.org/10.1016/j.envpol.2020.114507

Cheng, Y.F., Su, H., Rose, D., Gunthe, S.S., Berghof, M., Wehner, B., Achtert, P., Nowak, A., Takegawa, N., Kondo, Y., Shiraiwa, M., Gong, Y.G., Shao, M., Hu, M., Zhu, T., Zhang, Y.H., Carmichael, G.R., Wiedensohler, A., Andreae, M.O., Pöschl, U., 2012. Size-resolved measurement of the mixing state of soot in the megacity Beijing, China: diurnal cycle, aging and parameterization. Atmospheric Chemistry and Physics 12, 4477–4491. https://doi.org/10.5194/acp-12-4477-2012

Chien, L.-C., Chen, L.-W.A., Lin, R.-T., 2022. Lagged meteorological impacts on COVID-19 incidence among high-risk counties in the United States—a spatiotemporal analysis. J Expo Sci Environ Epidemiol 32, 774–781. https://doi.org/10.1038/s41370-021-00356-y

Clemente, Á., Yubero, E., Nicolás, J.F., Caballero, S., Crespo, J., Galindo, N., 2022. Changes in the concentration and composition of urban aerosols during the COVID-19 lockdown. Environmental Research 203, 111788. https://doi.org/10.1016/j.envres.2021.111788

Cui, S., Xian, J., Shen, F., Zhang, L., Deng, B., Zhang, Y., Ge, X., 2021. One-Year Real-Time Measurement of Black Carbon in the Rural Area of Qingdao, Northeastern China: Seasonal Variations, Meteorological Effects, and the COVID-19 Case Analysis. Atmosphere 12, 394. https://doi.org/10.3390/atmos12030394

Cui, Y., Ji, D., Maenhaut, W., Gao, W., Zhang, R., Wang, Y., 2020. Levels and sources of hourly PM2.5-related elements during the control period of the COVID-19 pandemic at a rural site between Beijing and Tianjin. Science of The Total Environment 744, 140840. https://doi.org/10.1016/j.scitotenv.2020.140840

Ding, A., Huang, X., Nie, W., Chi, X., Xu, Zheng, Zheng, L., Xu, Zhengning, Xie, Y., Qi, X., Shen, Y., Sun, P., Wang, J., Wang, L., Sun, J., Yang, X.-Q., Qin, W., Zhang, X., Cheng, W., Liu, W., Pan, L., Fu, C., 2019. Significant reduction of $PM_{2.5}$ in eastern China due to regional-scale emission control: evidence from SORPES in 2011–2018. Atmospheric Chemistry and Physics 19, 11791–11801. https://doi.org/10.5194/acp-19-11791-2019

Ding, S., Liu, D., Hu, K., Zhao, D., Tian, P., Wang, F., Li, R., Chen, Y., He, H., Huang, M., Ding, D., 2021. Optical and hygroscopic properties of black carbon influenced by particle microphysics at the top of the anthropogenically polluted boundary layer. Atmospheric Chemistry & Physics 21, 681–694. https://doi.org/10.5194/acp-21-681-2021

Feng, Z., Zheng, F., Liu, Y., Fan, X., Yan, C., Zhang, Y., Daellenbach, K.R., Bianchi, F., Petäjä, T., Kulmala, M., Bao, X., 2022. Evolution of organic carbon during COVID-19 lockdown period: Possible contribution of nocturnal chemistry. Sci Total Environ 808, 152191. https://doi.org/10.1016/j.scitotenv.2021.152191

Ge, B., Xu, D., Wild, O., Yao, X., Wang, J., Chen, X., Qixin, T., Pan, X., Wang, Z., 2020. Inter-annual variations of wet deposition in Beijing during 2014–2017:

645   implications of below-cloud scavenging of inorganic aerosols.
646   https://doi.org/10.5194/acp-2020-1146

647 Gorelick, N., Hancher, M., Dixon, M., Ilyushchenko, S., Thau, D., Moore, R., 2017.
648   Google Earth Engine: Planetary-scale geospatial analysis for everyone. Remote
649   Sensing of Environment, Big Remotely Sensed Data: tools, applications and
650   experiences 202, 18–27. https://doi.org/10.1016/j.rse.2017.06.031

651 He, C., Liou, K.-N., Takano, Y., Zhang, R., Levy Zamora, M., Yang, P., Li, Q., Leung,
652   L.R., 2015. Variation of the radiative properties during black carbon aging:
653   theoretical and experimental intercomparison. Atmospheric Chemistry and
654   Physics 15, 11967–11980. https://doi.org/10.5194/acp-15-11967-2015

655 Hopke, P.K., Gao, N., Cheng, M.-D., 1993. Combining chemical and meteorological
656   data to infer source areas of airborne pollutants. Chemometrics and Intelligent
657   Laboratory Systems, Proceedings of the 5th Conference on Computer
658   Applications in Analytical Chemistry (COMPANA '92) 19, 187–199.
659   https://doi.org/10.1016/0169-7439(93)80103-O

660 Huang, X., Ding, A., Gao, J., Zheng, B., Zhou, D., Qi, X., Tang, R., Wang, J., Ren, C.,
661   Nie, W., Chi, X., Xu, Z., Chen, L., Li, Y., Che, F., Pang, N., Wang, H., Tong, D.,
662   Qin, W., Cheng, W., Liu, W., Fu, Q., Liu, B., Chai, F., Davis, S.J., Zhang, Q.,
663   He, K., 2021. Enhanced secondary pollution offset reduction of primary
664   emissions during COVID-19 lockdown in China. Natl Sci Rev 8, nwaa137.
665   https://doi.org/10.1093/nsr/nwaa137

666 Huang, X., Wang, Z., Ding, A., 2018. Impact of Aerosol-PBL Interaction on Haze
667   Pollution: Multiyear Observational Evidences in North China. Geophysical
668   Research Letters 45, 8596–8603. https://doi.org/10.1029/2018GL079239

669 Isokääntä, S., Kim, P., Mikkonen, S., Kühn, T., Kokkola, H., Yli-Juuti, T., Heikkinen,
670   L., Luoma, K., Petäjä, T., Kipling, Z., Partridge, D., Virtanen, A., 2022. The
671   effect of clouds and precipitation on the aerosol concentrations and composition
672   in a boreal forest environment. Atmospheric Chemistry and Physics 22, 11823–
673   11843. https://doi.org/10.5194/acp-22-11823-2022

674 Jacobson, M.Z., 2002. Analysis of aerosol interactions with numerical techniques for
675   solving coagulation, nucleation, condensation, dissolution, and reversible
676   chemistry among multiple size distributions. Journal of Geophysical Research:
677   Atmospheres 107, AAC 2-1-AAC 2-23. https://doi.org/10.1029/2001JD002044

678 Jain, C.D., Madhavan, B.L., Singh, V., Prasad, P., Sai Krishnaveni, A., Ravi Kiran, V.,
679   Venkat Ratnam, M., 2021. Phase-wise analysis of the COVID-19 lockdown
680   impact on aerosol, radiation and trace gases and associated chemistry in a
681   tropical rural environment. Environmental Research 194, 110665.
682   https://doi.org/10.1016/j.envres.2020.110665

683 Jeong, C.-H., Yousif, M., Evans, G.J., 2022. Impact of the COVID-19 lockdown on the
684   chemical composition and sources of urban PM2.5. Environmental Pollution
685   292, 118417. https://doi.org/10.1016/j.envpol.2021.118417

686 Kahnert, M., 2010. On the Discrepancy between Modeled and Measured Mass

Absorption Cross Sections of Light Absorbing Carbon Aerosols. Aerosol Science and Technology 44, 453–460. https://doi.org/10.1080/02786821003733834

Kandler, K., Schneiders, K., Ebert, M., Hartmann, M., Weinbruch, S., Prass, M., Pöhlker, C., 2018. Composition and mixing state of atmospheric aerosols determined by electron microscopy: method development and application to aged Saharan dust deposition in the Caribbean boundary layer. Atmospheric Chemistry and Physics 18, 13429–13455. https://doi.org/10.5194/acp-18-13429-2018

Kondo, Y., Matsui, H., Moteki, N., Sahu, L., Takegawa, N., Kajino, M., Zhao, Y., Cubison, M.J., Jimenez, J.L., Vay, S., Diskin, G.S., Anderson, B., Wisthaler, A., Mikoviny, T., Fuelberg, H.E., Blake, D.R., Huey, G., Weinheimer, A.J., Knapp, D.J., Brune, W.H., 2011. Emissions of black carbon, organic, and inorganic aerosols from biomass burning in North America and Asia in 2008. Journal of Geophysical Research: Atmospheres 116. https://doi.org/10.1029/2010JD015152

Laughner, J.L., Neu, J.L., Schimel, D., Wennberg, P.O., Barsanti, K., Bowman, K.W., Chatterjee, A., Croes, B.E., Fitzmaurice, H.L., Henze, D.K., Kim, J., Kort, E.A., Liu, Z., Miyazaki, K., Turner, A.J., Anenberg, S., Avise, J., Cao, H., Crisp, D., de Gouw, J., Eldering, A., Fyfe, J.C., Goldberg, D.L., Gurney, K.R., Hasheminassab, S., Hopkins, F., Ivey, C.E., Jones, D.B.A., Liu, J., Lovenduski, N.S., Martin, R.V., McKinley, G.A., Ott, L., Poulter, B., Ru, M., Sander, S.P., Swart, N., Yung, Y.L., Zeng, Z.-C., 2021. Societal shifts due to COVID-19 reveal large-scale complexities and feedbacks between atmospheric chemistry and climate change. Proc Natl Acad Sci U S A 118, e2109481118. https://doi.org/10.1073/pnas.2109481118

Le, T., Wang, Y., Liu, L., Yang, J., Yung, Y.L., Li, G., Seinfeld, J.H., 2020. Unexpected air pollution with marked emission reductions during the COVID-19 outbreak in China. Science 369, 702–706. https://doi.org/10.1126/science.abb7431

Li, J., Jiang, L., Chen, C., Liu, D., Du, S., Zhang, Y., Yang, Y., Tang, L., 2020. Characteristics and Sources of Black Carbon Aerosol in a Mega-City in the Western Yangtze River Delta, China. Atmosphere 11, 315. https://doi.org/10.3390/atmos11040315

Li, K., Wang, X., Lu, X., Chen, H., Yang, X., 2022. Effects of Volatile Components on Mixing State and Size Distribution of Individual Black Carbon Aerosols. Aerosol Air Qual. Res. 22, 210400. https://doi.org/10.4209/aaqr.210400

Li, L., Huang, Z., Dong, J., Li, M., Gao, W., Nian, H., Fu, Z., Zhang, G., Bi, X., Cheng, P., Zhou, Z., 2011. Real time bipolar time-of-flight mass spectrometer for analyzing single aerosol particles. International Journal of Mass Spectrometry 303, 118–124. https://doi.org/10.1016/j.ijms.2011.01.017

Li, L., Li, Q., Huang, L., Wang, Q., Zhu, A., Xu, J., Liu, Ziyi, Li, H., Shi, L., Li, R., Azari, M., Wang, Y., Zhang, X., Liu, Zhiqiang, Zhu, Y., Zhang, K., Xue, S., Ooi,

729   M.C.G., Zhang, D., Chan, A., 2020. Air quality changes during the COVID-19 lockdown over the Yangtze River Delta Region: An insight into the impact of human activity pattern changes on air pollution variation. Science of The Total Environment 732, 139282. https://doi.org/10.1016/j.scitotenv.2020.139282

Liu, D., Joshi, R., Wang, J., Yu, C., Allan, J.D., Coe, H., Flynn, M.J., Xie, C., Lee, J., Squires, F., Kotthaus, S., Grimmond, S., Ge, X., Sun, Y., Fu, P., 2019. Contrasting physical properties of black carbon in urban Beijing between winter and summer. Atmospheric Chemistry and Physics 19, 6749–6769. https://doi.org/10.5194/acp-19-6749-2019

Liu, Q., Jing, B., Peng, C., Tong, S., Wang, W., Ge, M., 2016. Hygroscopicity of internally mixed multi-component aerosol particles of atmospheric relevance. Atmospheric Environment 125, 69–77. https://doi.org/10.1016/j.atmosenv.2015.11.003

Luo, J., Li, Z., Zhang, C., Zhang, Q., Zhang, Yongming, Zhang, Ying, Curci, G., Chakrabarty, R.K., 2022. Regional impacts of black carbon morphologies on shortwave aerosol–radiation interactions: a comparative study between the US and China. Atmospheric Chemistry and Physics 22, 7647–7666. https://doi.org/10.5194/acp-22-7647-2022

Moffet, R.C., Rödel, T.C., Kelly, S.T., Yu, X.Y., Carroll, G.T., Fast, J., Zaveri, R.A., Laskin, A., Gilles, M.K., 2013. Spectro-microscopic measurements of carbonaceous aerosol aging in Central California. Atmospheric Chemistry and Physics 13, 10445–10459. https://doi.org/10.5194/acp-13-10445-2013

Morcrette, J.-J., Boucher, O., Jones, L., Salmond, D., Bechtold, P., Beljaars, A., Benedetti, A., Bonet, A., Kaiser, J.W., Razinger, M., Schulz, M., Serrar, S., Simmons, A.J., Sofiev, M., Suttie, M., Tompkins, A.M., Untch, A., 2009. Aerosol analysis and forecast in the European Centre for Medium-Range Weather Forecasts Integrated Forecast System: Forward modeling. Journal of Geophysical Research: Atmospheres 114. https://doi.org/10.1029/2008JD011235

Nie, D., Shen, F., Wang, J., Ma, X., Li, Z., Ge, P., Ou, Y., Jiang, Y., Chen, Meijuan, Chen, Mindong, Wang, T., Ge, X., 2021. Changes of air quality and its associated health and economic burden in 31 provincial capital cities in China during COVID-19 pandemic. Atmos Res 249, 105328. https://doi.org/10.1016/j.atmosres.2020.105328

Peng, J., Hu, M., Guo, S., Du, Z., Zheng, Jing, Shang, D., Levy Zamora, M., Zeng, L., Shao, M., Wu, Y.-S., Zheng, Jun, Wang, Y., Glen, C.R., Collins, D.R., Molina, M.J., Zhang, R., 2016. Markedly enhanced absorption and direct radiative forcing of black carbon under polluted urban environments. Proceedings of the National Academy of Sciences 113, 4266–4271. https://doi.org/10.1073/pnas.1602310113

Polissar, A.V., Hopke, P.K., Paatero, P., Kaufmann, Y.J., Hall, D.K., Bodhaine, B.A., Dutton, E.G., Harris, J.M., 1999. The aerosol at Barrow, Alaska: long-term

771 trends and source locations. Atmospheric Environment 33, 2441–2458.
772 https://doi.org/10.1016/S1352-2310(98)00423-3

773 Qin, M., Hu, A., Mao, J., Li, X., Sheng, L., Sun, J., Li, J., Wang, X., Zhang, Y., Hu, J.,
774 2021. PM2.5 and O3 relationships affected by the atmospheric oxidizing
775 capacity in the Yangtze River Delta, China. Science of The Total Environment
776 152268. https://doi.org/10.1016/j.scitotenv.2021.152268

777 Ramanathan, V., Carmichael, G., 2008. Global and regional climate changes due to
778 black carbon. Nature Geoscience 1, 221–227. https://doi.org/10.1038/ngeo156

779 Sedlacek, A.J., Lewis, E.R., Onasch, T.B., Zuidema, P., Redemann, J., Jaffe, D.,
780 Kleinman, L.I., 2022. Using the Black Carbon Particle Mixing State to
781 Characterize the Lifecycle of Biomass Burning Aerosols. Environ. Sci. Technol.
782 56, 14315–14325. https://doi.org/10.1021/acs.est.2c03851

783 Silva, P.J., Liu, D.-Y., Noble, C.A., Prather, K.A., 1999. Size and Chemical
784 Characterization of Individual Particles Resulting from Biomass Burning of
785 Local Southern California Species. Environ. Sci. Technol. 33, 3068–3076.
786 https://doi.org/10.1021/es980544p

787 Song, X.-H., Hopke, P.K., Fergenson, D.P., Prather, K.A., 1999. Classification of Single
788 Particles Analyzed by ATOFMS Using an Artificial Neural Network, ART-2A.
789 Anal. Chem. 71, 860–865. https://doi.org/10.1021/ac9809682

790 Steinfeld, J.I., 1998. Atmospheric Chemistry and Physics: From Air Pollution to
791 Climate Change. Environment: Science and Policy for Sustainable
792 Development 40, 26–26. https://doi.org/10.1080/00139157.1999.10544295

793 Sulaymon, I.D., Zhang, Yuanxun, Hopke, P.K., Hu, J., Zhang, Yang, Li, L., Mei, X.,
794 Gong, K., Shi, Z., Zhao, B., Zhao, F., 2021a. Persistent high PM2.5 pollution
795 driven by unfavorable meteorological conditions during the COVID-19
796 lockdown period in the Beijing-Tianjin-Hebei region, China. Environmental
797 Research 198, 111186. https://doi.org/10.1016/j.envres.2021.111186

798 Sulaymon, I.D., Zhang, Yuanxun, Hopke, P.K., Zhang, Yang, Hua, J., Mei, X., 2021b.
799 COVID-19 pandemic in Wuhan: Ambient air quality and the relationships
800 between criteria air pollutants and meteorological variables before, during, and
801 after lockdown. Atmospheric Research 250, 105362.
802 https://doi.org/10.1016/j.atmosres.2020.105362

803 Sun, J., Sun, Y., Xie, C., Xu, Weiqi, Chen, C., Wang, Zhe, Li, L., Du, X., Huang, F., Li,
804 Y., Li, Z., Pan, X., Ma, N., Xu, Wanyun, Fu, P., Wang, Zifa, 2022. The chemical
805 composition and mixing state of BC-containing particles and the implications
806 on light absorption enhancement. Atmos. Chem. Phys. 22, 7619–7630.
807 https://doi.org/10.5194/acp-22-7619-2022

808 Sun, J., Wang, Zhe, Zhou, W., Xie, C., Wu, C., Chen, C., Han, T., Wang, Q., Li, Z., Li,
809 J., Fu, P., Wang, Zifa, Sun, Y., 2021. Measurement report: Long-term changes
810 in black carbon and aerosol optical properties from 2012 to 2020 in Beijing,
811 China (preprint). Aerosols/Field Measurements/Troposphere/Physics (physical
812 properties and processes). https://doi.org/10.5194/acp-2021-637

813 Sun, Y., Du, W., Fu, P., Wang, Q., Li, J., Ge, X., Zhang, Q., Zhu, C., Ren, L., Xu, W.,
814   Zhao, J., Han, T., Worsnop, D.R., Wang, Z., 2016. Primary and secondary
815   aerosols in Beijing in winter: sources, variations and processes. Atmos. Chem.
816   Phys.

817 Sun, Y., Lei, L., Zhou, W., Chen, C., He, Y., Sun, J., Li, Z., Xu, W., Wang, Q., Ji, D., Fu,
818   P., Wang, Z., Worsnop, D.R., 2020. A chemical cocktail during the COVID-19
819   outbreak in Beijing, China: Insights from six-year aerosol particle composition
820   measurements during the Chinese New Year holiday. Science of The Total
821   Environment 742, 140739. https://doi.org/10.1016/j.scitotenv.2020.140739

822 Taylor, J.W., Allan, J.D., Allen, G., Coe, H., Williams, P.I., Flynn, M.J., Le Breton, M.,
823   Muller, J.B.A., Percival, C.J., Oram, D., Forster, G., Lee, J.D., Rickard, A.R.,
824   Parrington, M., Palmer, P.I., 2014. Size-dependent wet removal of black carbon
825   in Canadian biomass burning plumes. Atmospheric Chemistry and Physics 14,
826   13755–13771. https://doi.org/10.5194/acp-14-13755-2014

827 Wang, H., Miao, Q., Shen, L., Yang, Q., Wu, Y., Wei, H., 2021. Air pollutant variations
828   in Suzhou during the 2019 novel coronavirus (COVID-19) lockdown of 2020:
829   High time-resolution measurements of aerosol chemical compositions and
830   source apportionment. Environmental Pollution 271, 116298.
831   https://doi.org/10.1016/j.envpol.2020.116298

832 Wang, J., Ge, X., Sonya, C., Ye, J., Lei, Y., Chen, M., Zhang, Q., 2022. Influence of
833   regional emission controls on the chemical composition, sources, and size
834   distributions of submicron aerosols: Insights from the 2014 Nanjing Youth
835   Olympic Games. Science of The Total Environment 807, 150869.
836   https://doi.org/10.1016/j.scitotenv.2021.150869

837 Wang, J., Liu, D., Ge, X., Wu, Y., Shen, F., Chen, M., Zhao, J., Xie, C., Wang, Q., Xu,
838   W., Zhang, J., Hu, J., Allan, J., Joshi, R., Fu, P., Coe, H., Sun, Y., 2019.
839   Characterization of black carbon-containing fine particles in Beijing during
840   wintertime. Atmos. Chem. Phys. 19, 447–458. https://doi.org/10.5194/acp-19-
841   447-2019

842 Wang, Pengfei, Chen, K., Zhu, S., Wang, Peng, Zhang, H., 2020. Severe air pollution
843   events not avoided by reduced anthropogenic activities during COVID-19
844   outbreak. Resources, Conservation and Recycling 158, 104814.
845   https://doi.org/10.1016/j.resconrec.2020.104814

846 Wang, Q., Liu, S., Zhou, Y., Cao, J., Han, Y., Ni, H., Zhang, N., Huang, R., 2015.
847   Characteristics of Black Carbon Aerosol during the Chinese Lunar Year and
848   Weekdays in Xi'an, China. Atmosphere 6, 195–208.
849   https://doi.org/10.3390/atmos6020195

850 Wang, S., Zhao, M., Xing, J., Wu, Y., Zhou, Y., Lei, Y., He, K., Fu, L., Hao, J., 2010.
851   Quantifying the Air Pollutants Emission Reduction during the 2008 Olympic
852   Games in Beijing. Environ. Sci. Technol. 44, 2490–2496.
853   https://doi.org/10.1021/es9028167

854 Wang, Y., Zhu, S., Ma, J., Shen, J., Wang, Pengfei, Wang, Peng, Zhang, H., 2021.

Enhanced atmospheric oxidation capacity and associated ozone increases during COVID-19 lockdown in the Yangtze River Delta. Science of The Total Environment 768, 144796. https://doi.org/10.1016/j.scitotenv.2020.144796

Wang, Y.Q., 2014. MeteoInfo: GIS software for meteorological data visualization and analysis. Meteorological Applications 21, 360–368. https://doi.org/10.1002/met.1345

Wang, Y.Q., Zhang, X.Y., Draxler, R.R., 2009. TrajStat: GIS-based software that uses various trajectory statistical analysis methods to identify potential sources from long-term air pollution measurement data. Environmental Modelling & Software 24, 938–939. https://doi.org/10.1016/j.envsoft.2009.01.004

WHO global air quality guidelines: Particulate matter (PM2.5 and PM10), ozone, nitrogen dioxide, sulfur dioxide and carbon monoxide, 2021. , WHO Guidelines Approved by the Guidelines Review Committee. World Health Organization, Geneva.

Xie, C., He, Y., Lei, L., Zhou, W., Liu, J., Wang, Q., Xu, W., Qiu, Y., Zhao, J., Sun, J., Li, L., Li, M., Zhou, Z., Fu, P., Wang, Z., Sun, Y., 2020. Contrasting mixing state of black carbon-containing particles in summer and winter in Beijing. Environmental Pollution 263, 114455. https://doi.org/10.1016/j.envpol.2020.114455

Xu, J., Ge, X., Zhang, X., Zhao, W., Zhang, R., Zhang, Y., 2020. COVID-19 Impact on the Concentration and Composition of Submicron Particulate Matter in a Typical City of Northwest China. Geophysical Research Letters 47, e2020GL089035. https://doi.org/10.1029/2020GL089035

Yang, J., Ma, S., Gao, B., Li, X., Zhang, Y., Cai, J., Li, M., Yao, L., Huang, B., Zheng, M., 2017. Single particle mass spectral signatures from vehicle exhaust particles and the source apportionment of on-line PM2.5 by single particle aerosol mass spectrometry. Science of The Total Environment 593–594, 310–318. https://doi.org/10.1016/j.scitotenv.2017.03.099

Zhang, G., Fu, Y., Peng, X., Sun, W., Shi, Z., Song, W., Hu, W., Chen, D., Lian, X., Li, L., Tang, M., Wang, X., Bi, X., 2021. Black Carbon Involved Photochemistry Enhances the Formation of Sulfate in the Ambient Atmosphere: Evidence From In Situ Individual Particle Investigation. Geophys Res Atmos 126. https://doi.org/10.1029/2021JD035226

Zhang, J., Li, H., Chen, L., Huang, X., Zhang, W., Zhao, R., 2022. Particle composition, sources and evolution during the COVID-19 lockdown period in Chengdu, southwest China: Insights from single particle aerosol mass spectrometer data. Atmospheric Environment 268, 118844. https://doi.org/10.1016/j.atmosenv.2021.118844

Zhang, J., Yuan, Q., Liu, L., Wang, Y., Zhang, Y., Xu, L., Pang, Y., Zhu, Y., Niu, H., Shao, L., Yang, S., Liu, H., Pan, X., Shi, Z., Hu, M., Fu, P., Li, W., 2021. Trans-Regional Transport of Haze Particles From the North China Plain to Yangtze River Delta During Winter. JGR Atmospheres 126.

897   https://doi.org/10.1029/2020JD033778

898 Zhang, K., Liu, Z., Zhang, X., Li, Q., Jensen, A., Tan, W., Huang, L., Wang, Y., de Gouw,
899   J., Li, L., 2022. Insights into the significant increase in ozone during COVID-
900   19 in a typical urban city of China. Atmos. Chem. Phys. 22, 4853–4866.
901   https://doi.org/10.5194/acp-22-4853-2022

902 Zhang, Y., Liu, X., Zhang, L., Tang, A., Goulding, K., Collett, J.L., 2021. Evolution of
903   secondary inorganic aerosols amidst improving PM2.5 air quality in the North
904   China plain. Environmental Pollution 281, 117027.
905   https://doi.org/10.1016/j.envpol.2021.117027

906 Zhang Y., Wang X., Chen H., Yang X., Chen J., Alien J.O., 2009. Source Apportionment
907   Of Lead-containing Aerosol Particles In Shanghai Using Single Particle Mass
908   Spectrometry. Chemosphere 74, 501–507.

909 Zhang, Y., Yuan, Q., Huang, D., Kong, S., Zhang, J., Wang, X., Lu, C., Shi, Z., Zhang,
910   X., Sun, Y., Wang, Z., Shao, L., Zhu, J., Li, W., 2018. Direct Observations of
911   Fine Primary Particles From Residential Coal Burning: Insights Into Their
912   Morphology, Composition, and Hygroscopicity. Journal of Geophysical
913   Research: Atmospheres 123, 12,964-12,979.
914   https://doi.org/10.1029/2018JD028988

915 Zhang, Z., Li, H., Ho, W., Cui, L., Men, Q., Cao, L., Zhang, Y., Wang, J., Huang, C.,
916   Lee, S., Huang, Y., Chen, M., Ge, X., 2024. Critical Roles of Surface-Enhanced
917   Heterogeneous Oxidation of SO2 in Haze Chemistry: Review of Extended
918   Pathways for Complex Air Pollution. Curr Pollution Rep.
919   https://doi.org/10.1007/s40726-023-00287-2

920 Zhou, H., Liu, T., Sun, B., Tian, Y., Zhou, X., Hao, F., Chun, X., Wan, Z., Liu, P., Wang,
921   J., Du, D., 2022. Chemical characteristics and sources of PM2.5 in Hohhot, a
922   semi-arid city in northern China: insight from the COVID-19 lockdown. Atmos.
923   Chem. Phys. 14.

924 Zhou, X., Gao, J., Wang, T., Wu, W., Wang, W., 2009. Measurement of black carbon
925   aerosols near two Chinese megacities and the implications for improving
926   emission inventories. Atmospheric Environment 43, 3918–3924.
927   https://doi.org/10.1016/j.atmosenv.2009.04.062

928 Zhou, Y., Wu, Y., Yang, L., Fu, L., He, K., Wang, S., Hao, J., Chen, J., Li, C., 2010. The
929   impact of transportation control measures on emission reductions during the
930   2008 Olympic Games in Beijing, China. Atmospheric Environment 44, 285–
931   293. https://doi.org/10.1016/j.atmosenv.2009.10.040

932 Zhu, X., Hu, B., Xin, J., Wang, L., Münkel, C., Mao, G., Wang, Y., 2015. Impact of
933   emission controls on air quality in Beijing during APEC 2014: Lidar ceilometer
934   observations. ATMOSPHERIC CHEMISTRY AND PHYSICS 15, 12667–
935   12680. https://doi.org/10.5194/acp-15-12667-2015
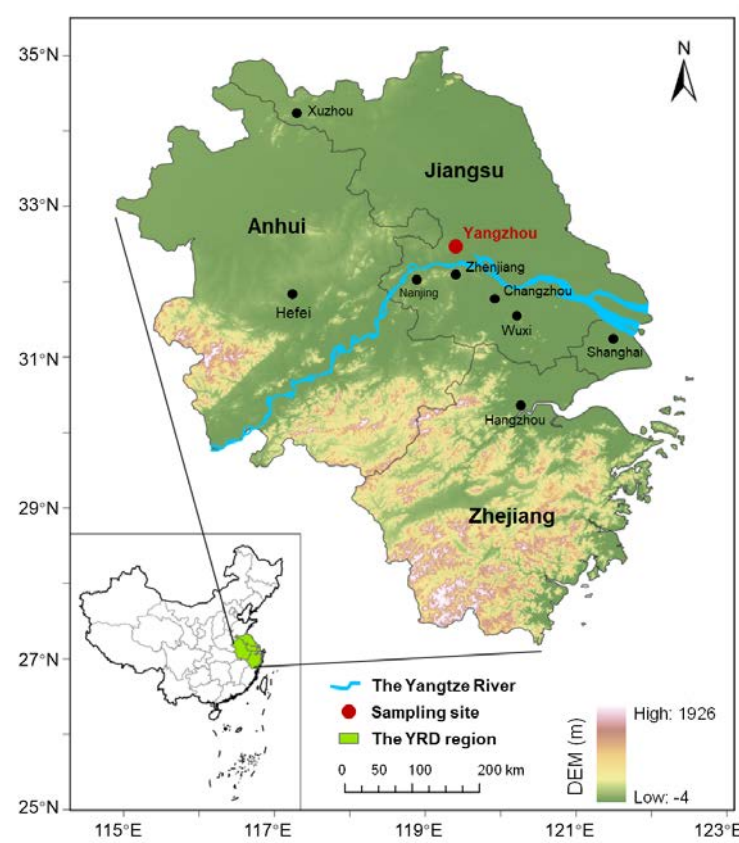
936

Figure 1. Geographical overview of the Yangtze River Delta (YRD) Region in China, depicting the major cities within the YRD and the sampling site located in Yangzhou. The color gradient from green to white indicates varying altitudes across the region (Maps were generated by using ArcGIS Pro).
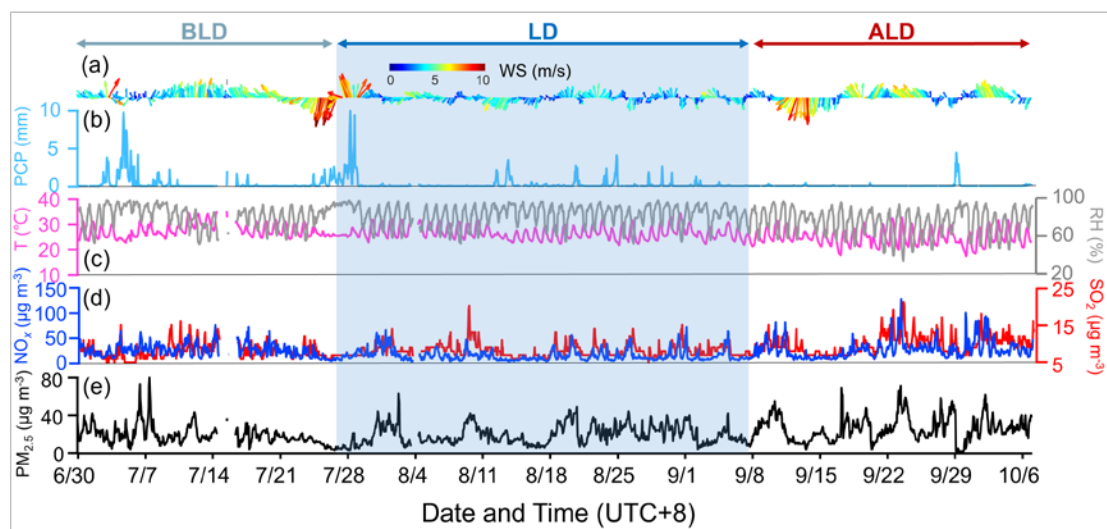

Figure 2. Temporal variations of **(a)** wind direction (WD) and wind speed (WS), **(b)** precipitation (PCP), **(c)** temperature (T) and relative humidity (RH), **(d)** concentrations of NO_x and SO_2, and **(e)** mass loading of $PM_{2.5}$. The blue-grey, dark-blue, and crimson arrow ranges denote the periods before lockdown (BLD), during lockdown (LD), and after lockdown (ALD).
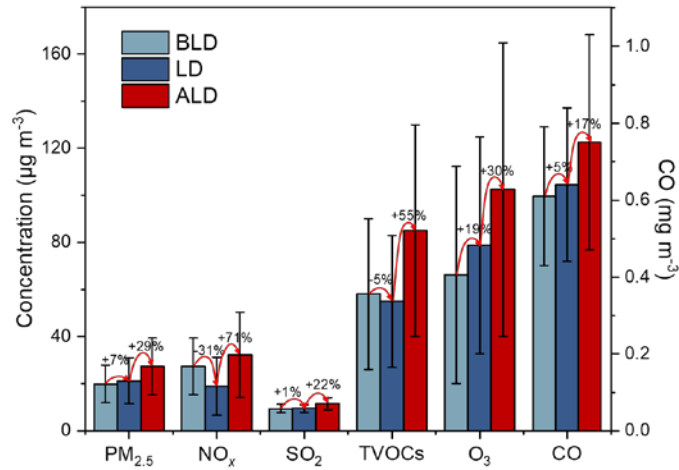
Figure 3. Ground-based observations of $PM_{2.5}$, NO_x, SO_2, O_3, CO, and TVOC concentrations in Yangzhou. The figure compares the averages during the BLD (blue-grey), LD (dark-blue), and ALD (crimson) periods. Error bars indicate SDs over different lockdown periods.
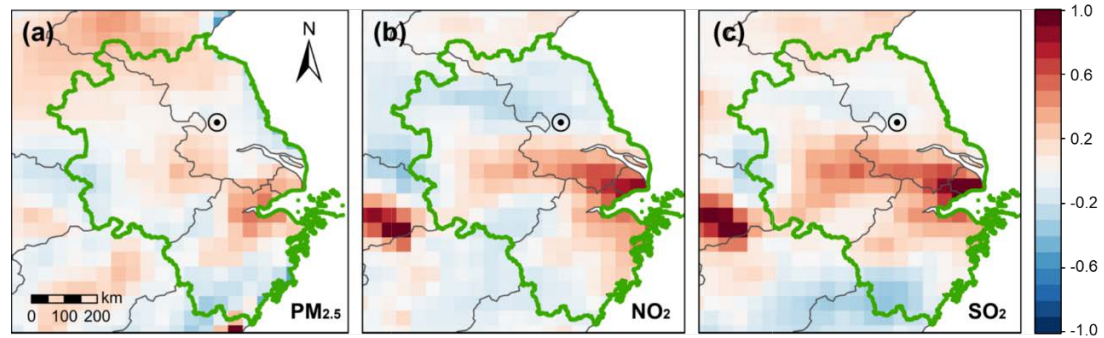

Figure 4. The fractional changes (i.e., (LD – BLD)/BLD) of **(a)** $PM_{2.5}$, **(b)** NO_2, and **(c)** SO_2 between BLD and LD periods based on spaceborne measurement. The circle symbols in the maps indicate the location of Yangzhou, and the green region represents the YRD.
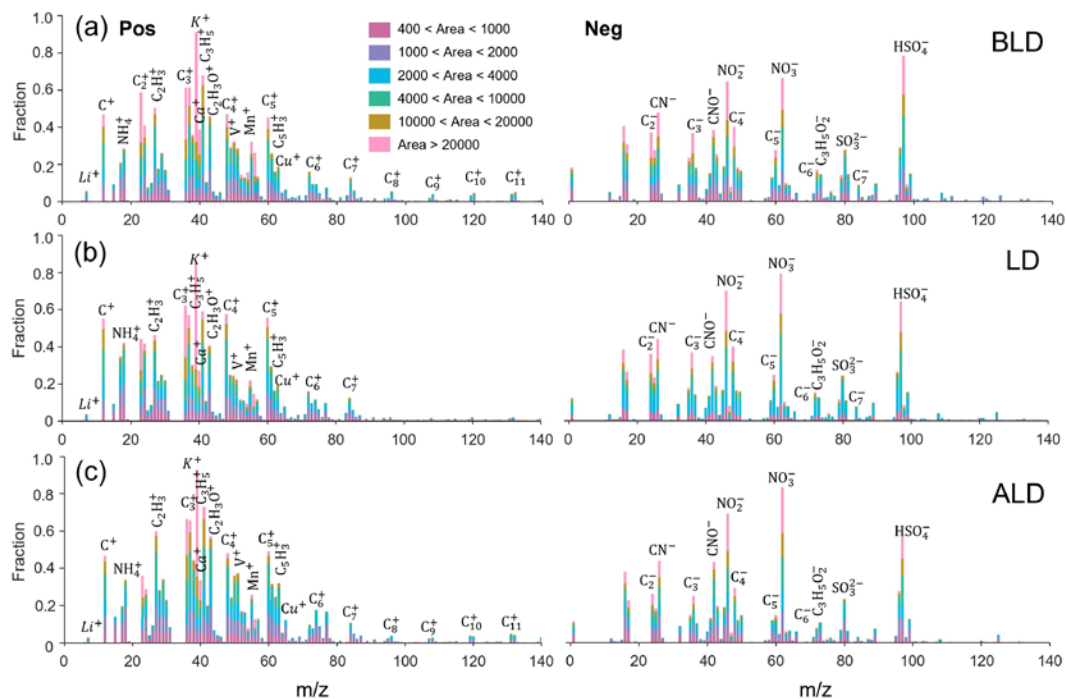
Figure 5. The average positive and negative mass spectra of BCc **(a)** before the lockdown period (BLD), **(b)** during the lockdown period (LD), and **(c)** after the lockdown period (ALD).

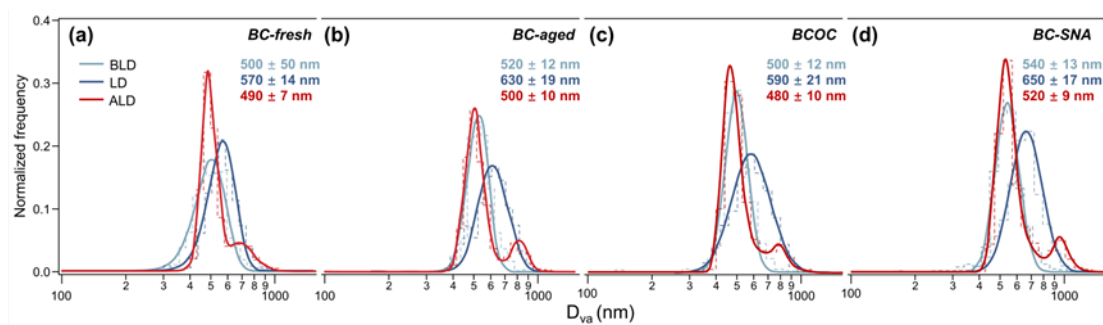**Figure 6.** Size distribution of different types of BCc during different periods in Yangzhou. **(a)** BC-fresh particles, **(b)** BC-aged particles, **(c)** BCOC particles, and **(d)** BC-SNA particles. The Log-normal distribution was used to fit the unimodal size distribution, and the Lorentz distribution was used to fit the bimodal size distribution. The corresponding mode sizes (with the standard deviations) are also shown.
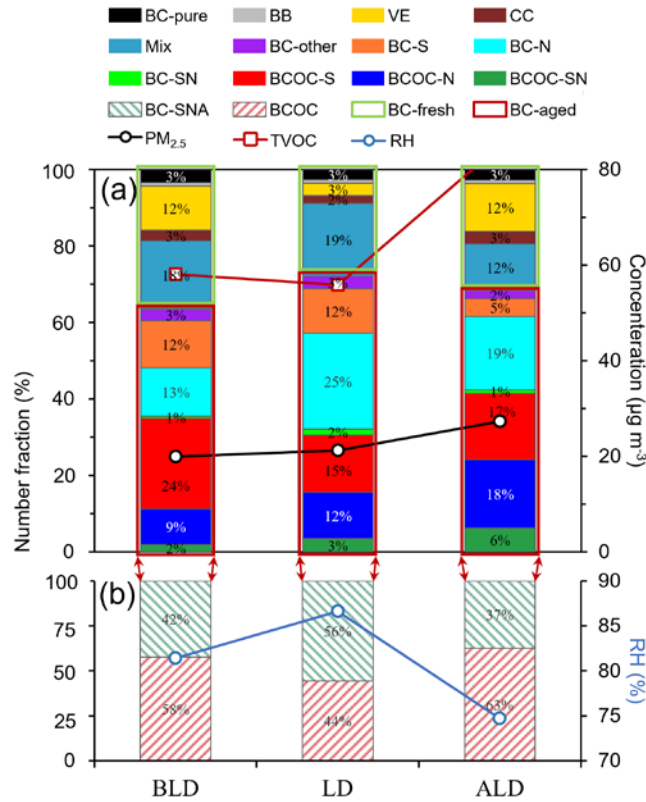
Figure 7. Number fractions of BCc. **(a)** The number fractions of different BCc along with the concentrations of PM$_{2.5}$ and total volatile organic compounds (TVOC). **(b)** The number fractions of different types of BC-aged particles along with relative humidity (RH).
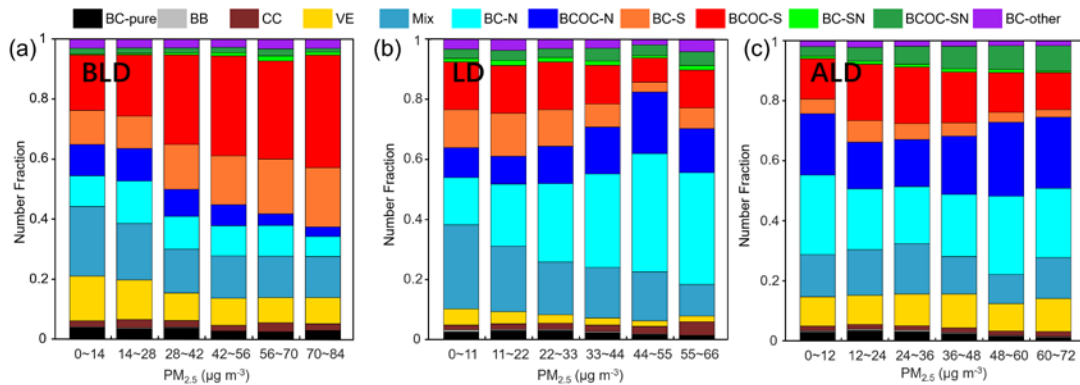

Figure 8. Variations of number fractions of BCc particle types with PM$_{2.5}$ mass concentrations during **(a)** the BLD period, **(b)** LD, and **(c)** the ALD period.
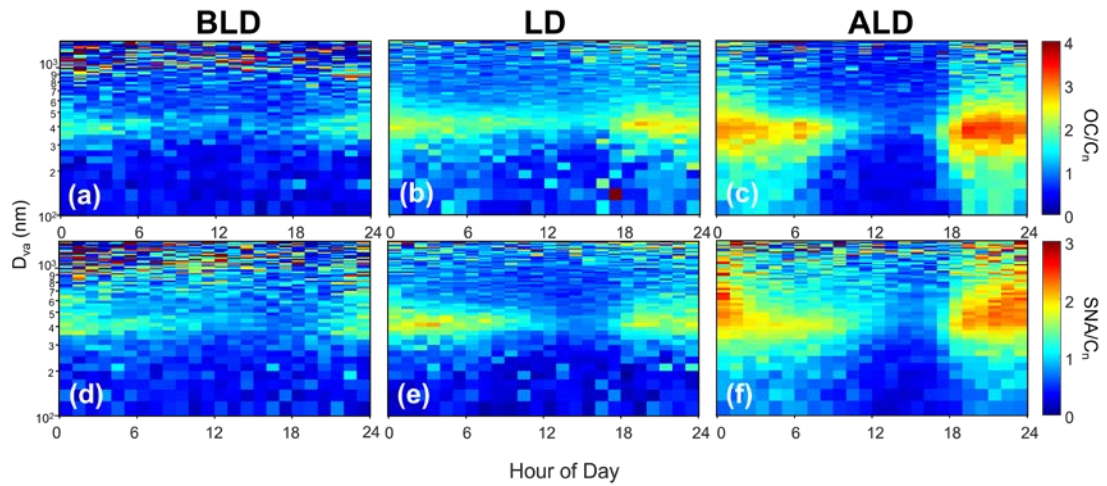
Figure 9. Diurnal variations of the ratios of OC/Cn and SNA/Cn with a size distribution of BCc during (**a, d**) BLD, (**b, e**) LD, and (**c, f**) ALD.
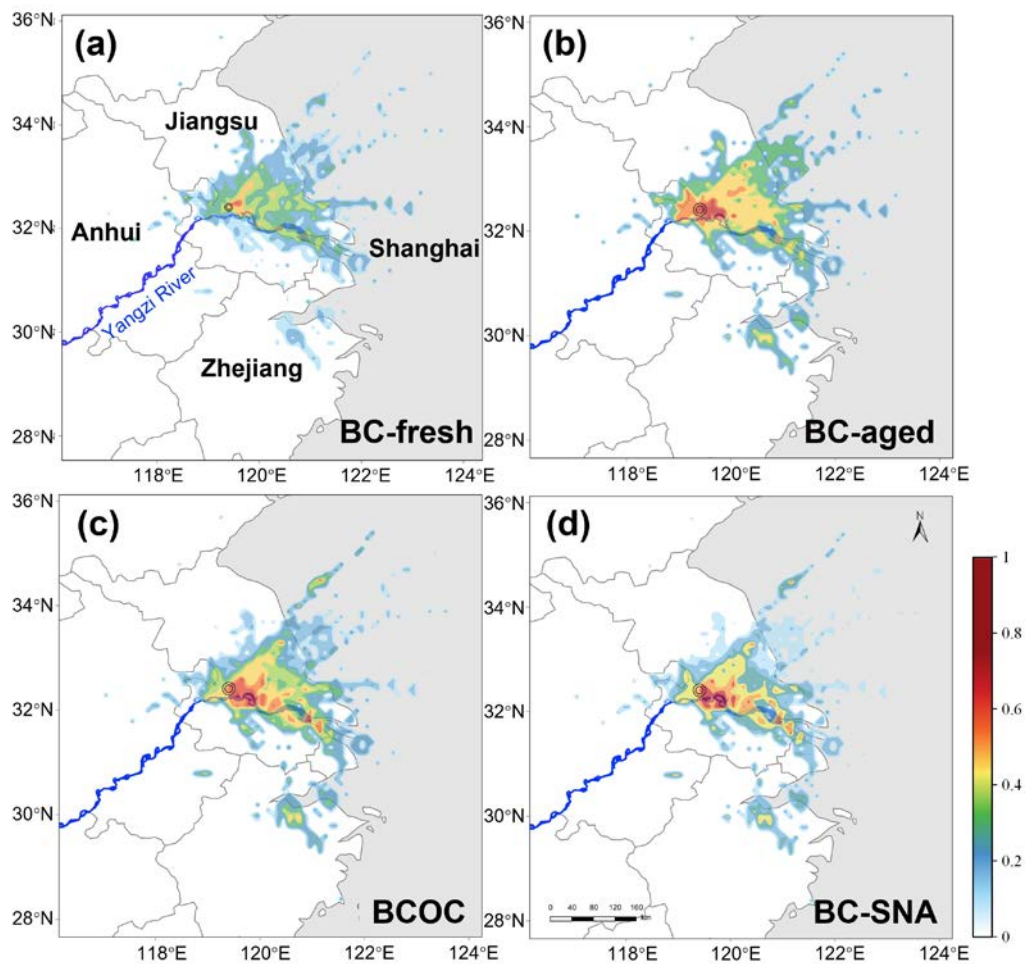

Figure 10. The PSCF maps for different BCc during LD. (**a**) BC-fresh. (**b**) BC-aged. (**c**) BCOC. (**d**) BC-SNA.